

NaCl-KCl-CaCl₂ molten salts for high temperature heat storage: Experimental and deep learning molecular dynamics simulation study

Xianqing Liu^a, Fei Liang^c, Shule Liu^a, Gechuanqi Pan^{b, **}, Jing Ding^{a, ***}, Jianfeng Lu^{a,*}

^a School of Materials Science and Engineering, Sun Yat-sen University, Guangzhou, 510006, PR China

^b School of Chemical Engineering and Energy Technology, Dongguan University of Technology, Dongguan, 523808, PR China

^c Department of Mechanical Engineering, City University of Hong Kong, Kowloon Tong, 999077, Hong Kong Special Administrative Region of China



ARTICLE INFO

Keywords:

High-temperature energy storage
NaCl-KCl-CaCl₂ molten salt
Thermophysical properties
Structure

ABSTRACT

The thermal energy storage system based on molten salts plays a crucial role in renewable energy utilization and power grid regulation system. This article investigates NaCl-KCl-CaCl₂ molten salts for high temperature heat storage by experimental measurement and deep learning molecular dynamics simulations. The phase transition, thermal stability, and thermophysical properties of NaCl-KCl-CaCl₂ were experimental analyzed, and the results indicate that it has high enthalpy of 251.37 J/g, with observable evaporation at temperatures above 1103 K. An accurate deep potential model was further trained based on ab initio molecular dynamics data, achieving a root mean square error of 0.50 meV/atom for energy and 15.31 meV/Å for force, and the experimental and computational results for density and viscosity have discrepancies of less than 5 %. Based on experimental and simulation data, correlation equations for thermophysical properties of NaCl-KCl-CaCl₂ were conducted, and thermal performance changes with temperature were further explained from the perspective of structural changes. As the temperature rises, all ionic pairs transfer to lower coordination numbers and disperse into smaller clusters, which results in the decreases of density, thermal conductivity and viscosity, and the stability of molten salt gradually decreases as the energy barriers for ion pairs dropping.

Nomenclature

C_p	Specific heat capacity
E	Potential energy
ΔF_f	Root mean square error of force.
M	Molar mass
N_A	Avogadro's constant
p_e	Energy prefactor
p_f	Force prefactor
R	Coordinate matrix
r	Radius
r_{\min}	The first peak valley
t	Time
Greek symbols	
ρ	Density
λ	Thermal conductivity
η	Shear viscosity
$\Delta \varepsilon$	Root mean square error of energy.
subscripts	
i	i ion

(continued on next column)

(continued)

Nomenclature	
j	j ion
k	k ion
x	X-axis direction
y	Y-axis direction
Hot	Heat source end
Cold	Cold source terminal
Abbreviations	
ADF	Bond angle distribution function
AIMD	Ab initio molecular dynamics simulation
CN	Coordination number
DFT	First molecular dynamics simulation
DP	Deep potential
DPMD	Deep learning molecular dynamics simulation
DSC	Differential scanning calorimetry
MSD	Root mean square displacement
RDF	Radial distribution function
RMSE	Root mean square error

(continued on next page)

* Corresponding author.

** Corresponding author.

*** Corresponding author.

E-mail addresses: pangechuanqi@163.com (G. Pan), dingjing@mail.sysu.edu.cn (J. Ding), lujfeng@mail.sysu.edu.cn (J. Lu).

(continued)

Nomenclature

RNEMD	Inverse non-equilibrium molecular dynamics
TGA	Thermogravimetric analysis

1. Introduction

In the context of diversified energy sources and the integration of new energy into the grid, grid stability faces significant challenges, particularly with the large-scale integration of wind and solar power, which introduces volatility and uncertainty. This forces traditional thermal power plants to enhance operational flexibility [1,2]. In this scenario, the development of large-scale, low-cost, and efficient energy storage technologies is key to optimizing the flexibility of traditional power plants. Thermal storage systems based on molten salt materials, with high heat capacity, environmental friendliness, and cost-effectiveness, have attracted widespread attention for their excellent thermal storage properties [3–6]. Research by Raud et al. [7] and Sau et al. [8] suggests that molten salts are suitable for heat storage, considering storage cost, efficiency, and thermal properties of the materials.

The thermal properties and structure of molten salts directly impact their performance and efficiency in energy storage systems. In our previous research [9], the thermal performance of NaCl-CaCl₂ molten salt was determined experimentally using thermal analysis methods. Wang et al. [10] found that after long-term high-temperature tests and multiple thermal cycling tests, the rate of change in the thermal properties of the molten salt is less than 10 %, demonstrating good thermal stability. Jacob et al. [11] found that molten salts exhibit excellent long-term

thermal stability. Studies by Na et al. [12,13] also support the long-term thermal stability of molten salts. These findings further endorse the feasibility of molten salts for high-temperature thermal storage; However their high operating temperatures, corrosiveness, and hygroscopicity [14–16] increase the difficulty of testing key thermal properties and microscopic structures, thereby adding to the complexity of the experiments.

In contemporary scientific research, molecular dynamics simulations have emerged as a vital tool for studying molten salts. Tian et al. [17] used molecular dynamics methods, revealing the local structural features and key thermal physical parameters. However, traditional classical molecular dynamics simulations are constrained by the setting of force field parameters, which often neglect the electronic polarization effect [18,19], thus limiting the accuracy of calculations. Although first-principles calculations excel in accuracy, their applicability is limited to small molecular systems [20]. The introduction of machine learning technology offers a new perspective to address this issue. Such technology strikes a balance between computational accuracy and efficiency, emerging as a promising direction for research [21]. The machine learning potential is supported by the conclusion of Xie et al. [22], whose calculation results are consistent with density functional theory (DFT). Dong et al. [23] used neural network machine learning methods to develop interatomic potentials for ternary chloride salts. Deep potential molecular dynamics (DPMD) simulations were conducted to predict the microstructure and thermophysical properties of the NaCl-MgCl₂-CaCl₂ ternary salt. Xie et al. [24] trained a machine learning potential function for the CaCl₂-NaCl system and successfully predicted the evolution of thermal physical parameters such as self-diffusion coefficients and thermal expansion coefficients. Overall, the Deep Potential Molecular Dynamics (DPMD) method based on machine learning potentials maintains computational accuracy while also considering computational speed.

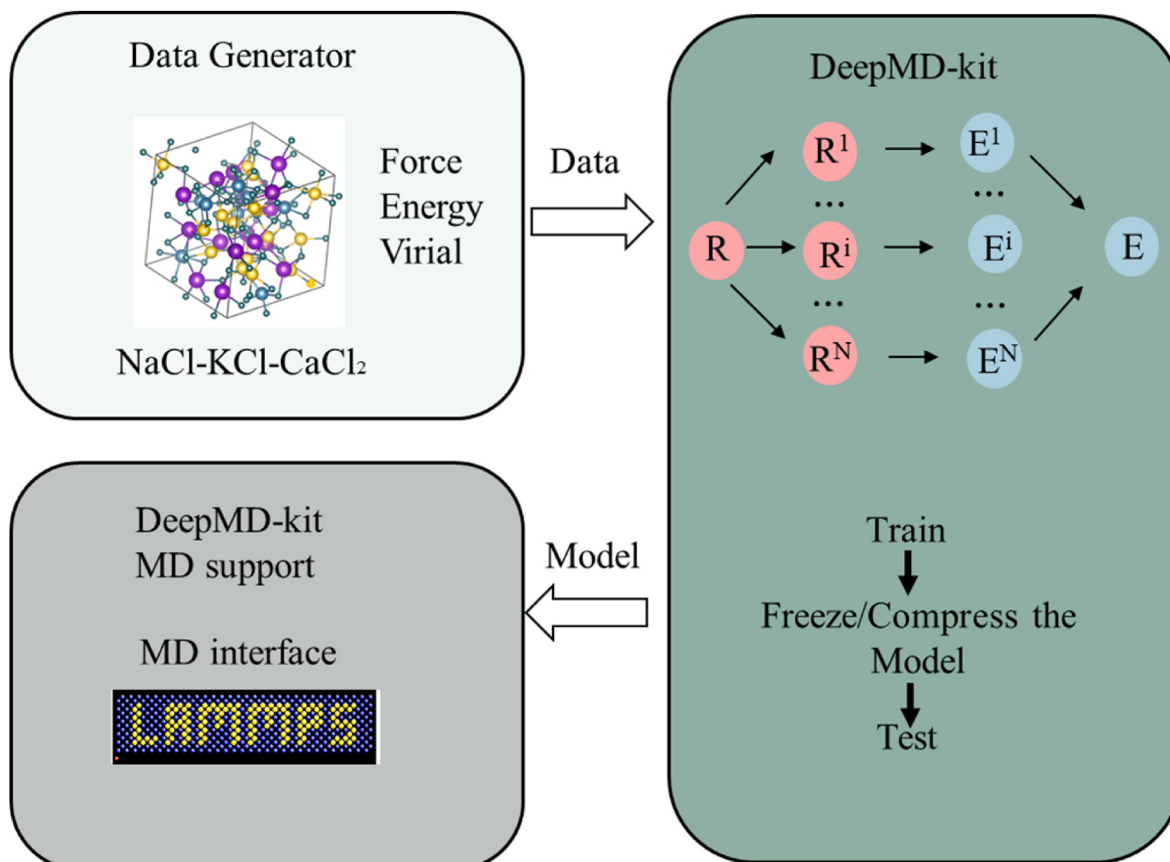


Fig. 1. The DPMD calculation process.

The chloride molten salt NaCl-KCl-CaCl₂ has become one of the most promising high-temperature heat storage materials due to its high operating temperature, high energy storage density, and low cost and environment-friendly. However, the thermophysical property data of NaCl-KCl-CaCl₂ mixed molten salt is still insufficient, and mature and accurate molecular dynamics potential function parameters is also lacked. In this paper, NaCl-KCl-CaCl₂ molten salts for high temperature heat storage was compressively researched by experimental measurement and deep learning molecular dynamics simulations. The phase transition, thermal stability, and thermophysical properties of the NaCl-KCl-CaCl₂ mixed molten salt were initially assessed. A deep potential for the NaCl-KCl-CaCl₂ system was then trained, and the structure parameters were analyzed using DPMD. The evolution of these structural parameters was further investigated, and the variations in density, thermal conductivity, and viscosity were predicted. These predictions were compared with experimental measurements to validate the reliability of DPMD. The results obtained are instrumental in propelling the development of molten salts for flexible retrofit and high-temperature thermal energy storage applications.

2. Experiment

2.1. Preparation

NaCl, KCl and CaCl₂ were purchased from Macklin Company and were analytically pure with purity $\geq 99.5\%$. Before preparation, NaCl, KCl and CaCl₂ were dehydrated in a 500 K electric blast drying oven for 24 h, and then the dried salt was evenly mixed and heated in a muffle e from room temperature to 1023 K, and kept at a constant temperature for 5 h to melt the sample. Finally, the prepared NaCl-CaCl₂-KCl (23.5-25-51.5 wt%) was cooled to 298 K and stored under seal for subsequent testing.

2.2. Material property testing

The melting point and latent heat of the NaCl-KCl-CaCl₂ mixed molten salt were determined primarily through TGA/DSC3+1HT testing. Approximately 15 mg of the sample was loaded into a platinum crucible and heated from 573 K to 973 K at a rate of 10 K/min, Argon environment with a flow rate of 50 ml/min.

Short-term thermal stability of the NaCl-KCl-CaCl₂ mixed molten salt was explored through thermogravimetric analysis, with the test temperature being heated from room temperature to 1273 K at a rate of 10 K/min, Argon environment with a flow rate of 50 ml/min. Additionally, 50 g of the NaCl-KCl-CaCl₂ mixed molten salt was subjected to a long-term stability test, Over the temperatures ranging from 923 K to 1223 K for 120 h, with weight changes recorded at 24-h intervals.

Specific heat capacity was measured using a SENSYS calorimeter. During testing, a 20 mg, equivalent in mass to sapphire, heated from room temperature to 1073 K, at a rate of 10 K/min, Argon environment with a flow rate of 10 ml/min.

Density testing was mainly based on the Archimedes method. The molten salt was heated from 298 K to 1103 K at a rate of 5 K/min, held at 1103 K for 2 h to stabilize the temperature, and then cooled at a rate of 1 K/min, with readings taken during the cooling process.

Viscosity was primarily tested using an MCR502 rheometer. Initially, the molten salt was heated to 1103 K, held for 2 h, and then cooled at a rate of 1 K/min, with shear rates set at 50 s⁻¹ for measurement.

3. Deep learning potential molecular dynamics simulation

3.1. Calculation process

In this study, the thermal properties and structure of NaCl-KCl-CaCl₂ molten salts were analyzed based on DPMD simulations. The DPMD calculation process is shown in Fig. 1, which mainly includes data

generation, model training, and DPMD simulation. An Energetic and Force dataset was first generated by AIMD. Then the DP model of NaCl-KCl-CaCl₂ was trained. Finally, the trained DP model was applied to predict changes in the microstructure and thermophysical properties.

3.1.1. Data preparation

The training dataset for machine learning is obtained through molecular dynamics simulations using ab initio simulation software (VASP) [25,26]. Initially, a model containing 109 atoms (15Na, 9 Ca, 26K, and 59 Cl). is constructed using packmol, simulations are performed at various temperatures under the NVT ensemble. The electron-nucleus interaction was represented by the projection-enhanced wave (PAW) method [27]. The electron exchange correlation, on the other hand, was described by the Perdew-Burke-Ernzerhof (PBE) method [28]. In addition, considering the van der Waals forces, the semi-empirical DFT-D2 method was employed [29–31]. The plane wave energy was set at 360 eV, with an energy convergence precision of 1.0×10^{-5} eV. A $1 \times 1 \times 1$ K-point mesh was used. Periodic boundary conditions and the Nosé-Hoover thermostat were applied to perform first-principles molecular simulation calculations. During the data preparation phase, for each target temperature (903K, 953K, 1003K, 1053K, 1103K), the calculation is carried out for 30 ps, with a time interval of 1 fs, resulting in 30,000 frames of data. Since there are five different target temperatures, a total of $30000 \times 5 = 150000$ frames of data are generated. 80 % of the data is allocated for training the deep potential (DP) model, while the remaining data is used for model validation.

3.1.2. Theoretical basis and DP training

The machine learning potential is trained using DEEPMOD-kit [32, 33]. A new potential is created by training the deep learning model with the dataset obtained from AIMD simulations. In DP training, the potential energy of each atom is built into the computational system [34]:

$$E = \sum_i E_i \quad (1)$$

Where i represents an atom, and Energy of an atom is determined by the position of the atom in which it is placed i and its surrounding atoms. E_i is defined as follow:

$$E_i = E_{s(i)}(R_i | \{R_j | j \in N_{rc}(i)\}) \quad (2)$$

where $s(i)$ represents the type of atom, $N_{rc}(i)$ is the surrounding atom of atom i , and R_i is the coordinate matrix of atom i .

In the DP training, the type of descriptor used is se_e2_a, with a smooth cutoff distance of 5.8 Å and a cutoff distance of 9.0 Å. The embedding and fitting neural networks are [25, 50, 100] and [240, 240, 240], respectively. The learning rate decay type is exponential, with an initial learning rate of 0.001 and a final learning rate of 1.0×10^{-8} . In terms of training configuration, the number of training steps is set to 1,000,000 steps.

Loss function was used to optimize parameters in machine learning. The loss function describes the error between DFT calculation and DP training.

$$L_f(p_e, p_f) = p_e \Delta \varepsilon^2 + \frac{p_f}{3N} \sum_i |\Delta F_i|^2 \quad (3)$$

Where p_e and p_f are the pre-factors for energy and force, respectively. In the early stages of training, force training dominates, with the pre-factor decreasing from 1000 to 1. In the later stages of training, energy training dominates, with the pre-factor increasing from 0.02 to 1. $\Delta \varepsilon$ and ΔF_i represent the root mean square errors (RMSE) for energy and force, respectively.

3.1.3. DPMD simulation

The trained machine learning model was integrated with the classical molecular simulation package LAMMPS to perform DPMD

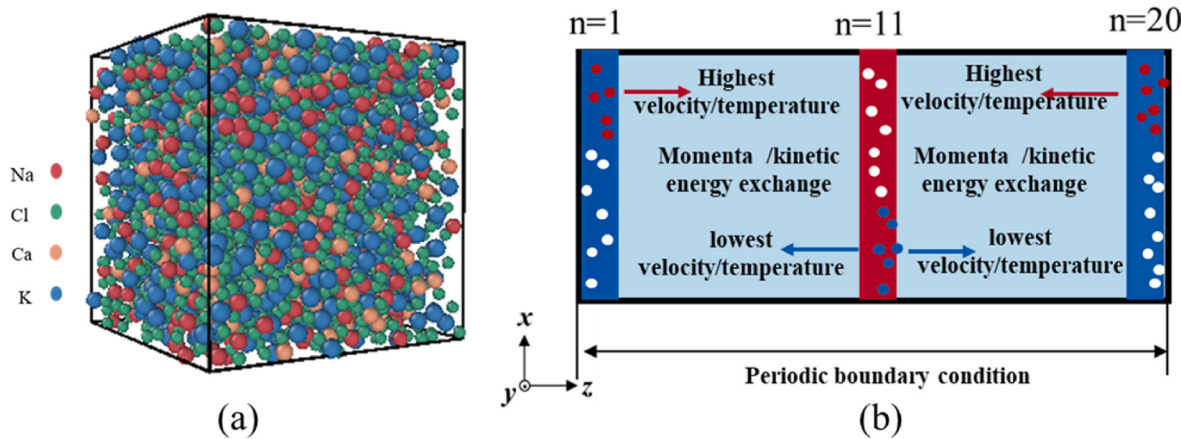


Fig. 2. (a) Molecular model, (b) Schematic diagram of shear viscosity/thermal conductivity calculated by RNEMD.

calculations. The molecular model, depicted in Fig. 2(a), consists of a total of 3102 ions, including 434 Na, 246 Ca, 748 K, and 1674 Cl ions. Firstly, the system was initially heated to 1500 K, then cooled down to target temperatures (903 K, 953 K, 1003 K, 1053 K, 1103 K), with a simulation time of 1 ns to capture local structural and density parameters. Subsequently, a 3 ns calculation was conducted under the NVT ensemble to determine shear viscosity and thermal conductivity. The calculation principle is shown in Fig. 2(b). Momentum or heat flux was applied along the direction of molten salt flow to achieve steady-state flow or establish a steady-state temperature gradient. Finally, shear

stress was calculated using Newtonian fluid shear stress formulas, thermal conductivity was calculated using Fourier's law of heat conduction.

3.2. Performance parameters

The thermal efficiency of thermal energy storage systems is crucial, where specific heat capacity and density are key parameters affecting the energy storage density. The system's heat transfer performance is significantly influenced by viscosity, self-diffusion coefficient, and

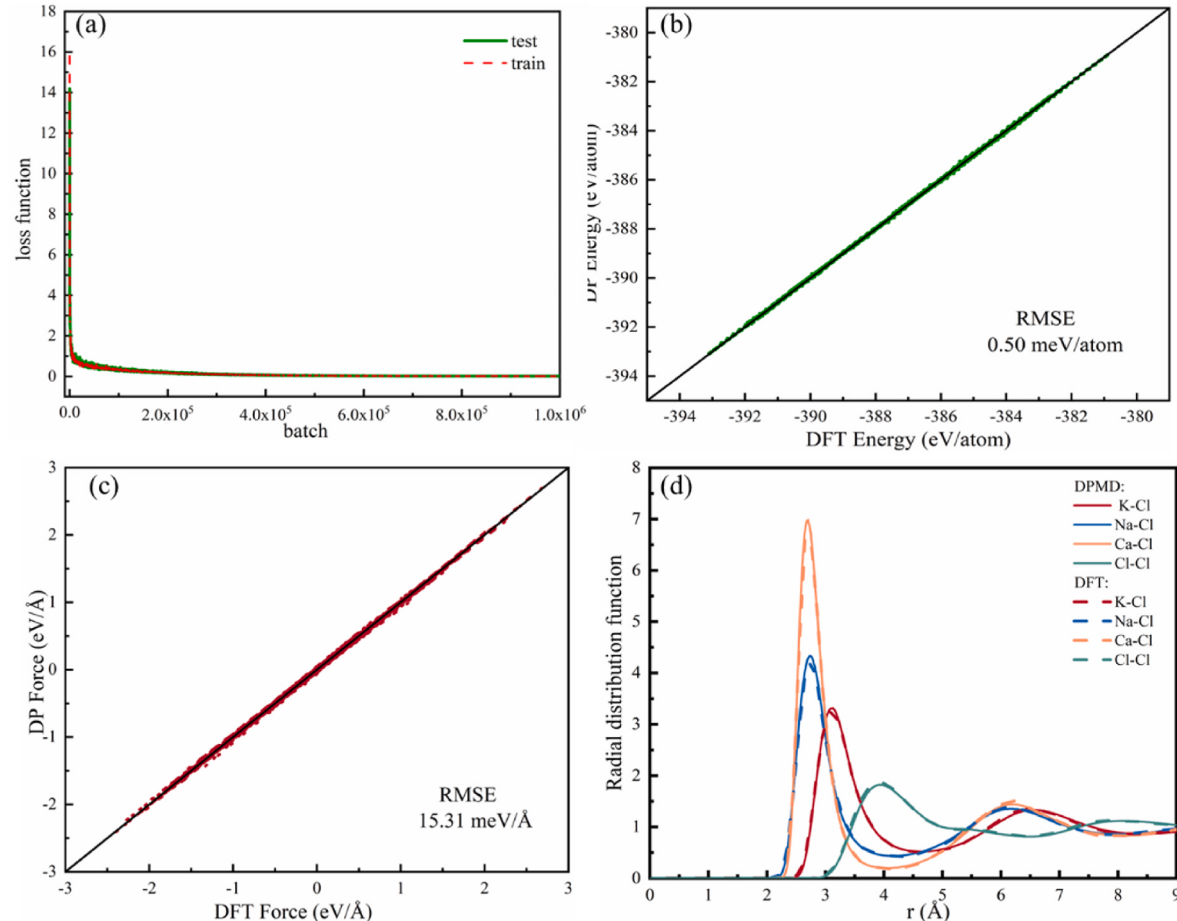


Fig. 3. (a) Changes of the loss function, (b) Energy predicted by DPMD and DFT, (c) Force predicted by DPMD and DFT, (d) RDF comparison of DPMD and DFT calculations.

thermal conductivity. The specific heat capacity and density were defined as Eqs. (4) and (5).

$$c_p = \left(\frac{\partial H}{\partial T} \right)_p \quad (4)$$

$$\rho = \frac{NM}{N_A V} \quad (5)$$

Here, N and M are the number of atoms and the molar mass, respectively, N_A is the Avogadro constant, and V is the volume after equilibrium. The viscosity, self-diffusion coefficient, and thermal conductivity were defined as Eqs. (6)–(9).

$$\eta = - \frac{\sum_{\text{transfer}} m(v_{\text{hot}} - v_{\text{cold}})}{2tL_x L_y (\partial v_x / \partial z)} \quad (6)$$

$$MSD(t) = \langle |\Delta r_i(t)|^2 \rangle = \frac{1}{N} \left(\sum_i |\mathbf{r}_i(t) - \mathbf{r}_i(0)|^2 \right) \quad (7)$$

$$D = \frac{1}{6} \lim_{t \rightarrow \infty} \frac{d(MSD)}{dt} \quad (8)$$

$$\lambda = - \frac{\sum_{\text{transfer}} \frac{m}{2} (v_{\text{hot}}^2 - v_{\text{cold}}^2)}{2tL_x L_y (\partial T / \partial z)} \quad (9)$$

Here, In Eq. (6), the numerator represents the momentum exchange value between the cold and hot ends, the denominator $\delta V_x / \delta Z$ is the velocity gradient along the Z-axis direction, and $L_x * L_y$ is the cross-sectional area of the box in the XY plane. In Eq. (6), $\Delta r_i(t)$ denotes the displacement of ion i over a time interval t , with the final value obtained by averaging. In Eq. (8), D is defined as the self-diffusion coefficient, which is calculated based on the Einstein equation using the mean square displacement over time; In Eq. (9), the numerator is defined as the kinetic energy exchange between the cold and hot ends, $\delta T / \delta Z$ represents the temperature gradient along the Z-axis direction, as before, $L_x * L_y$ denotes the cross-sectional area of the box in the XY plane. To further reveal the structural evolution inside the molten salt, the radial distribution functions (RDF), coordination number (CN), Angle distribution function and Potential of mean force of were employed, defined as Eqs. 10–13.

$$g_{ij}(r) = \frac{1}{4\pi\rho_j r^2} \left[\frac{dN_{ij}(r)}{dr} \right] \quad (10)$$

$$N_{ij} = 4\pi\rho_j \int_0^{r_{\min}} g_{ij}(r) r^2 dr \quad (11)$$

$$\theta_{ijk}(r) = \langle \cos^{-1} \left(\frac{r_{ij}^2 + r_{ik}^2 - r_{jk}^2}{2r_{ij}r_{ik}} \right) \rangle \quad (12)$$

Where i and j denote the ion type, respectively, sphere radius r . In Eq. (10),

N_{ij} represents the average number of ion j within a spherical radius r around ion i , and ρ_j is the number density of ion j . In Eq. (11), r_{\min} corresponds to the position of the first minimum in the RDF curve.

3.3. Validation of the DP model

To verify the accuracy of the DP (Deep Potential) trained model, the loss function of DP model was evaluated, along with the root mean square error (RMSE) of predicted energies and forces compared to DFT calculations. The relationship between the training step size of the DP model and the loss function is illustrated in Fig. 3(a). After 200,000 iterations, the training loss function aligns closely with the testing loss function, converging towards zero, indicating that 1,000,000 training steps are sufficient to ensure the stability and accuracy of the DP training

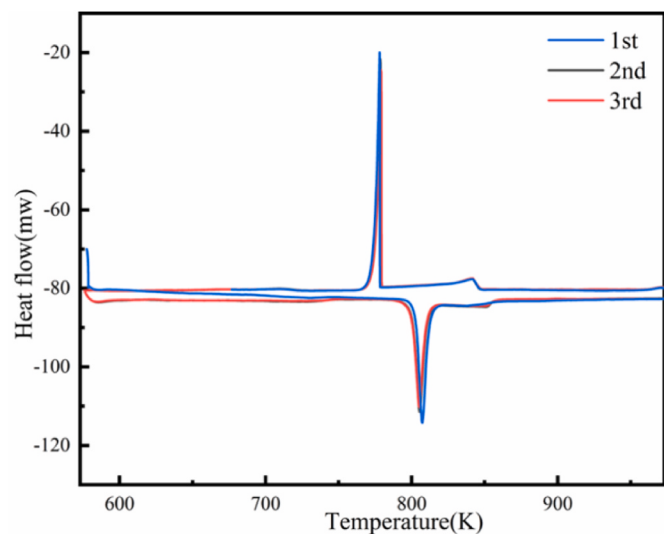


Fig. 4. DSC curve of NaCl-KCl-CaCl₂ mixed molten salt.

Table 1
Melting point and latent heat of NaCl-KCl-CaCl₂.

NaCl-KCl-CaCl ₂ (wt%)	Melting temperature (K)	Difference (%)	Latent heat (J/g)	Difference (%)
Average	777		251.37	/
1-cycle	780	+0.39	248.45	-1.17
2-cycle	776	-0.13	253.29	+0.76
3-cycle	775	-0.26	252.37	+0.4

model. Further comparison of the RMSE between the DP model and DFT predictions for energies and forces is depicted in Fig. 3(b) and (c), with respective RMSE values of 0.50 meV/atom and 15.31 meV/Å. This demonstrates that the DP training model can achieve predictive accuracy comparable to DFT. The radial distribution functions (RDFs) is shown in Fig. 3(d), where the RDF trajectories from DPMD simulations are consistent with those from DFT, with nearly identical peak positions and values for ion pairs. The trained DP model is capable of accurately predicting the local structure of the NaCl-KCl-CaCl₂ system.

4. Results and discussion

4.1. Thermal analysis

4.1.1. Phase transition analysis and latent heat

Fig. 4 presents the DSC thermogram of the NaCl-KCl-CaCl₂ mixed molten salt, The repeatability of the three cycles is good, with specific melting points, latent heats, and other information provided in Table 1. The average melting point from the three measurements is 777K, with the maximum deviation being +0.39 %; the latent heat is taken as the average value of 251.37 J/g, with an error less than ±1.2 %.

4.1.2. Stability analysis

Fig. 5(a) presents the TGA curve for the NaCl-KCl-CaCl₂ mixed molten salt. Initially, at 500K, a slight decrease (<0.3 %) in the thermogravimetric curve is observed, which may be attributed to the evaporation of moisture present in the molten salt. Upon reaching 1103 K, a mass loss of 3 % is recorded. As the temperature is further increased to 1103 K, the mass loss reaches 5.0 %. Subsequently, there is an intensification in the weight change of the sample, indicating that the molten salt can operate at a maximum temperature of 1103 K. In thermal power plant peak shaving energy storage, molten salts are utilized as thermal storage media and are required to operate at high temperatures for extended periods within sealed molten salt tanks. Therefore, A

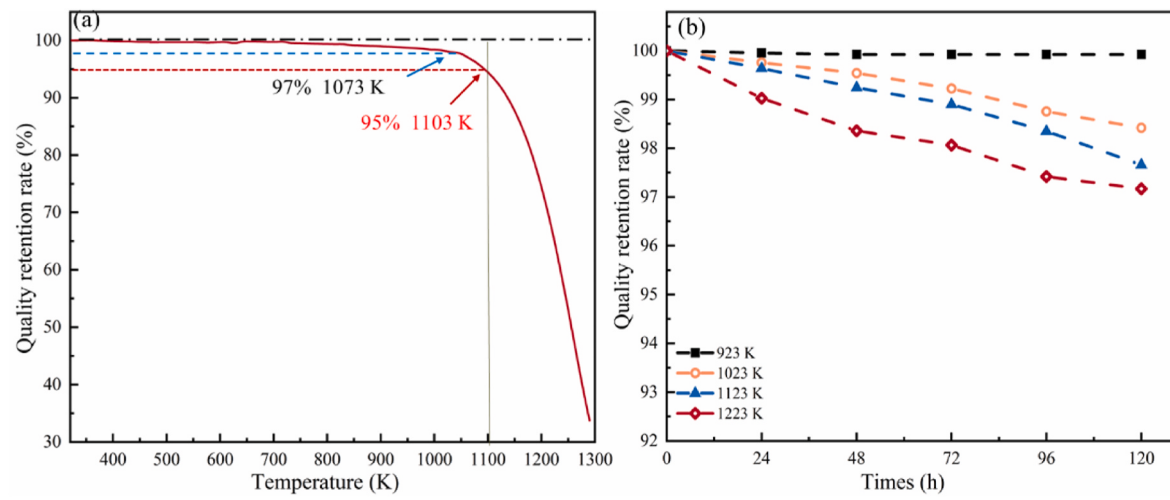


Fig. 5. (a) TGA curve, (b) Thermal stability.

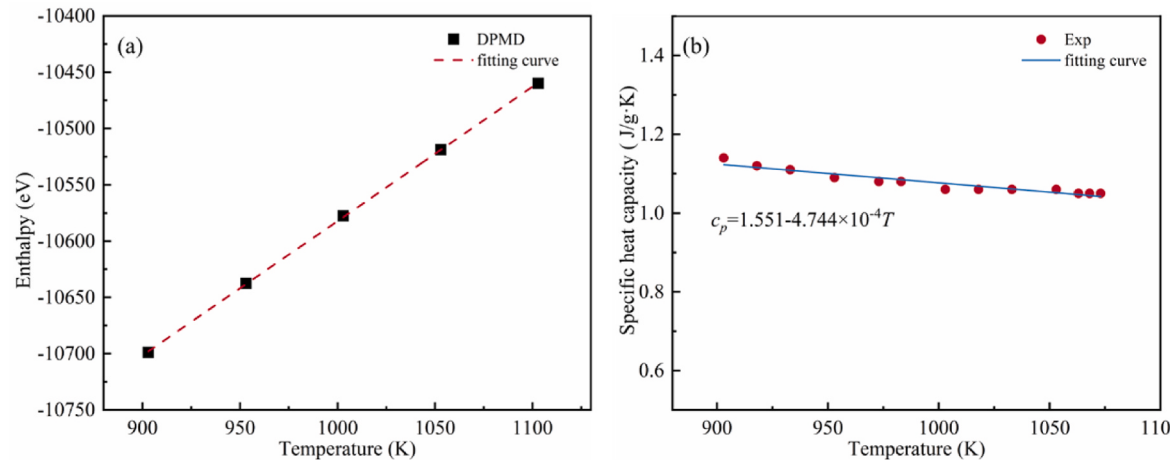


Fig. 6. (a) Enthalpy-temperature relationship, (b) Specific heat capacity.

Table 2
Specific heat capacity.

Methods	c_p (J/g·K)	Difference
Exp by this work(1003K)	1.09	/
DPMD by this work(1003K)	1.06	2.8 %
Exp by Yin [35]	0.9701	11.0 %
Exp by Kenisarin [36]	1.0	8.3 %

study on molten salt thermal stability in a high-temperature sealed setting was conducted. These salts were subjected to a 120-h stability test at temperatures ranging from 923 K to 1223 K. The results, as depicted in Fig. 5(b), show weight loss percentages of 0.078 %, 1.58 %, 2.34 %, and 2.83 % within the temperature range of 923 K–1223 K, respectively. This indicates that the NaCl-KCl-CaCl₂ mixed molten salt exhibits exceptional thermal stability.

4.2. Thermal physical property analysis

4.2.1. Specific heat capacity

Fig. 6(a) presents the enthalpy-temperature relationship as derived from DPMD simulations. The linear regression analysis yields a high coefficient of determination ($R^2 = 0.999$), indicative of an excellent fit. This empirical linearity implies that the specific heat capacity at constant pressure can be approximated as a constant value over the studied

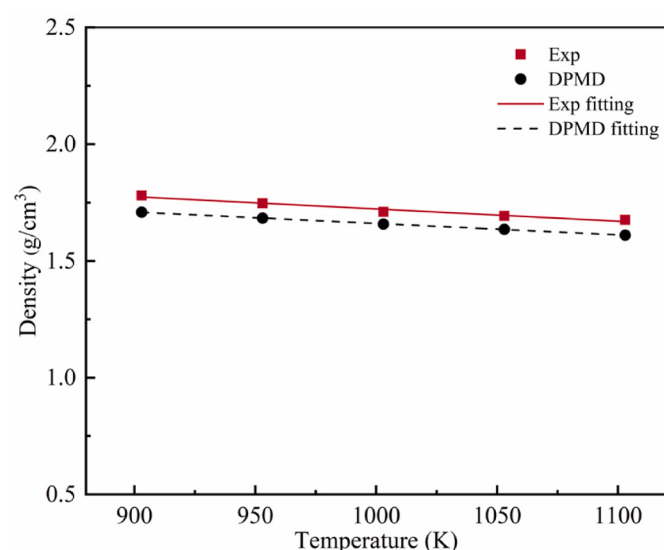


Fig. 7. Density variation curve, where the red solid squares and black solid dots represent the experimental and DPMD calculated values, respectively. The red solid line is the linear fit for the experimental data, and the black dashed line is the linear fit for the DPMD calculated data.

Table 3
Density of mixture salt by DPMD and experimental.

Compose	Density(g/cm ³)
DPMD(this work)	$\rho(\text{g}/\text{cm}^3) = 2.152 - 4.9115 \times 10^{-4}T$
Exp(this work)	$\rho(\text{g}/\text{cm}^3) = 2.248 - 5.244 \times 10^{-4}T$

temperature range. The specific heat capacity thus calculated is reported to be 1.060 J/g·K, Fig. 6(b) presents the result of experiment, with an average specific heat of 1.09 J/g·K in the temperature range of 903 K–1103 K. The result is further validated through a rigorous comparison with other experimental data, as shown in Table 2, revealing a minimal error margin of 2.8 %. Such a discrepancy between the computed and experimental values substantiates the accuracy and reliability of the DPMD simulation approach.

4.2.2. Density

A comparative analysis is conducted between DPMD and experimental. The computational densities are obtained from averaging over a 200 ps timeframe, as illustrated in Fig. 7. It is observed that across the thermal gradient of 903 K–1103 K, the density exhibits a decremental trend with rising temperature. This behavior can be correlated with the structural transformations detailed in subsequent discourse, where the augmented kinetic energy of ions at elevated temperatures engenders an expansion of the interionic spacing. The maximal deviation of the DPMD-simulated densities from experiment data is confined to less than 4.0 %, thereby reflecting a substantial alignment among the datasets. Such consistency serves to validate the precision of the DP model.

The simulated densities by DPMD, manifesting lower values within the 903 K–1103 K range, could be ascribed to the approximations inherent in the scattering corrections and exchange-correlation potentials employed in the DFT simulations that precede the DPMD data preparation [37]. The temperature-dependent evolution of both DPMD-simulated and experimental densities has been subjected to regression analysis, with the pertinent equations delineated in Table 3. The regression coefficients are 0.9996 for the DPMD dataset and 0.9837 for the empirical dataset, underscoring the robustness of the fitting procedures.

4.2.3. Shear viscosity

During the viscosity calculation, box size was defined as a cube with a side length of 48 Å, and the z-direction was magnified by a factor of 2,

giving the system a length of 96 Å in the z-direction. In addition, our previous study found no size effect for viscosity calculation using RNEMD [38]; therefore, the size effect in the z-axis is not investigated in depth here. In the calculation process, it is divided into 20 regions along the z-axis direction, the first region is defined as the cold source region, and the 11th region is defined as the heat source region. Furthermore, the momentum exchange frequency adopted is set to 100 and the calculation time interval is 1 fs. For chloride molten salts, an exchange time of 100 fs is sufficient to meet the requirement of linear changes in momentum exchange and kinetic energy exchange [39,40]. Therefore, we did not deeply explore the effect of switching frequency. It can also be seen from the results in Fig. 8(a) that in the calculation process of molten salt viscosity, the total calculation time of 3 ns and a momentum exchange of 100 fs can meet the requirements of linear momentum change. Therefore, the results of our study are credible. Furthermore, by comparing the experimental and calculated results, as shown in Fig. 8(b), we can find that the shear viscosity calculated by DPMD decreases

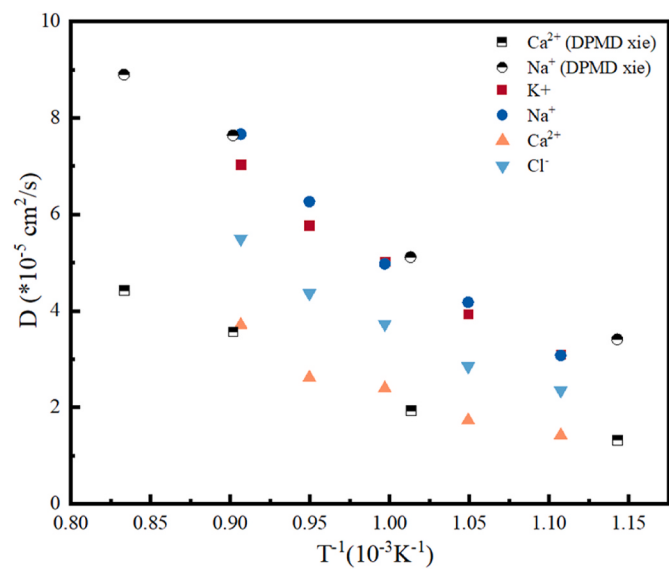


Fig. 9. Self-diffusion coefficients at different temperatures. DPMD calculated values are represented by solid symbols, Semi-solid circles and squares were calculated by Xie [22].

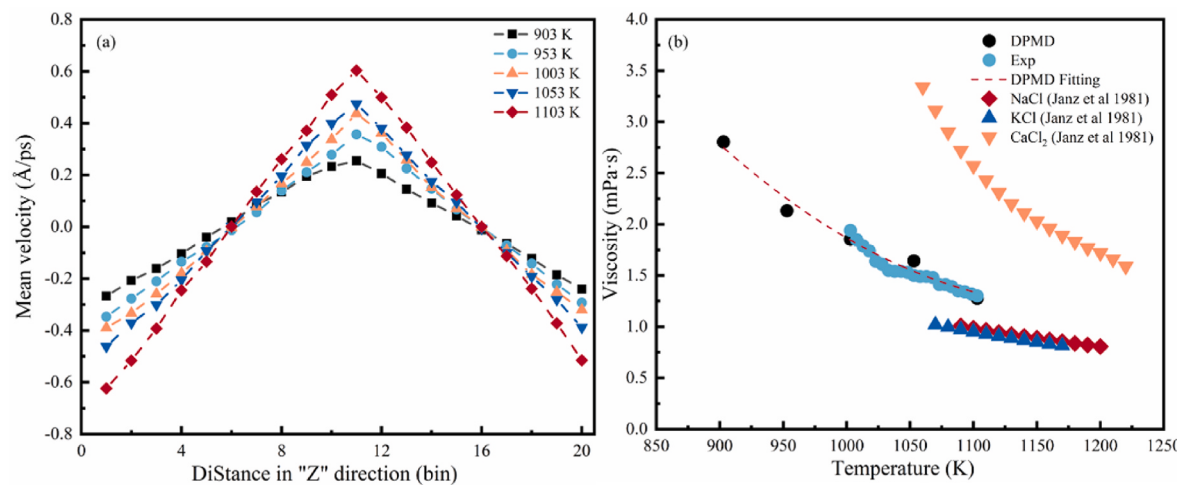


Fig. 8. (a) Mean velocity gradient at different temperatures. The dashed line represents the linear fitting of velocity. (b) Viscosity-temperature relationship curve for the NaCl-KCl-CaCl₂ molten salt, where the black and blue solid circles represent the DPMD and experimental viscosity values, respectively. The red dashed line is the fitting curve for the DPMD viscosity calculation. The solid red squares, blue upward triangles, and orange downward triangles represent the experimental viscosity values for the individual salts NaCl, KCl, and CaCl₂ [41], respectively.

Table 4

Self-diffusion coefficient parameters fitted by the Arrhenius equation.

Ions	E_a (kJ/mol)	e_a (eV)	D_0	T (K)
K ⁺	33.61	0.348	274.51	903–1103
Na ⁺	36.97	0.383	429.23	903–1103
Ca ²⁺	38.55	0.400	233.92	903–1103
Cl ⁻	35.17	0.365	249.14	903–1103

from 2.804 mPa s to 1.277 mPa s in the temperature range of 903K–1103K. The experimental results show that the viscosity increases from 1.30 mPa s to 1.94 mPa s as the temperature decreases from 1103K to 1003K. The shear viscosity has a negative relationship with temperature. This is mainly due to the fact that the high temperature weakens the interaction between ions, which can be explained in conjunction with the structural analysis in the subsequent sections, as shown in Fig. 11. The deviation between the experimental and calculated results is controlled within 5 %, which indicates that DPMD has good accuracy in predicting thermophysical properties. Compared with Janz's [41] previous viscosity per unit salt, the viscosity of the molten salt prepared is within the range of per unit salt. The function relationship between shear viscosity and temperature is given by Eq. (13), and the fitting coefficient is 0.9792.

$$\ln \eta(mPa \cdot s) = -3.0313 + 3653.44/T \quad (13)$$

4.2.4. The self-diffusion coefficient

Fig. 9 shows the self-diffusion coefficient within the NaCl-KCl-CaCl₂ molten salt matrix, which is positively correlated with temperature. In the studied temperature range, the diffusion coefficient of Na ion increases from 3.0779×10^{-5} to 7.6616×10^{-5} , and the diffusion coefficient of K ion increases from 3.0973×10^{-5} to 7.0351×10^{-5} . The Cl ion was 2.3476×10^{-5} to 5.4937×10^{-5} , and the Ca ion was 1.4182×10^{-5} to 3.7098×10^{-5} . In addition, the self-diffusion coefficient equations of each ion were fitted based on the Arrhenius square, in the form shown in Eq. (14), and the specific parameters are shown in Table 4. Furthermore, a comparative examination of Xie's [22] research reveals that the discrepancy in ion self-diffusion coefficients is negligible within the investigated temperature spectrum.

$$D = D_0 \exp(-E_a / RT) = D_0 \exp(-\epsilon_a / kT) \quad (14)$$

4.2.5. Thermal conductivity

As shown in Fig. 10(a) and (b). The Length of supercell and convergence are performed at 1053 K, and the temperature gradient is linearly distributed for Z = NX (N = 1, 2, 3). Further thermal conductivity results show that when Z = X, the thermal conductivity is 0.3250, Z = 2X is 0.42103, and Z = 3X is 0.4295, which indicates that there is a certain size effect in the calculation of thermal conductivity, but from Z = 2X to Z = 3X, the thermal conductivity fluctuates very little and basically has reached convergence. Due to the limitation of computing resources and computational memory, we adopt Z = 2X for further

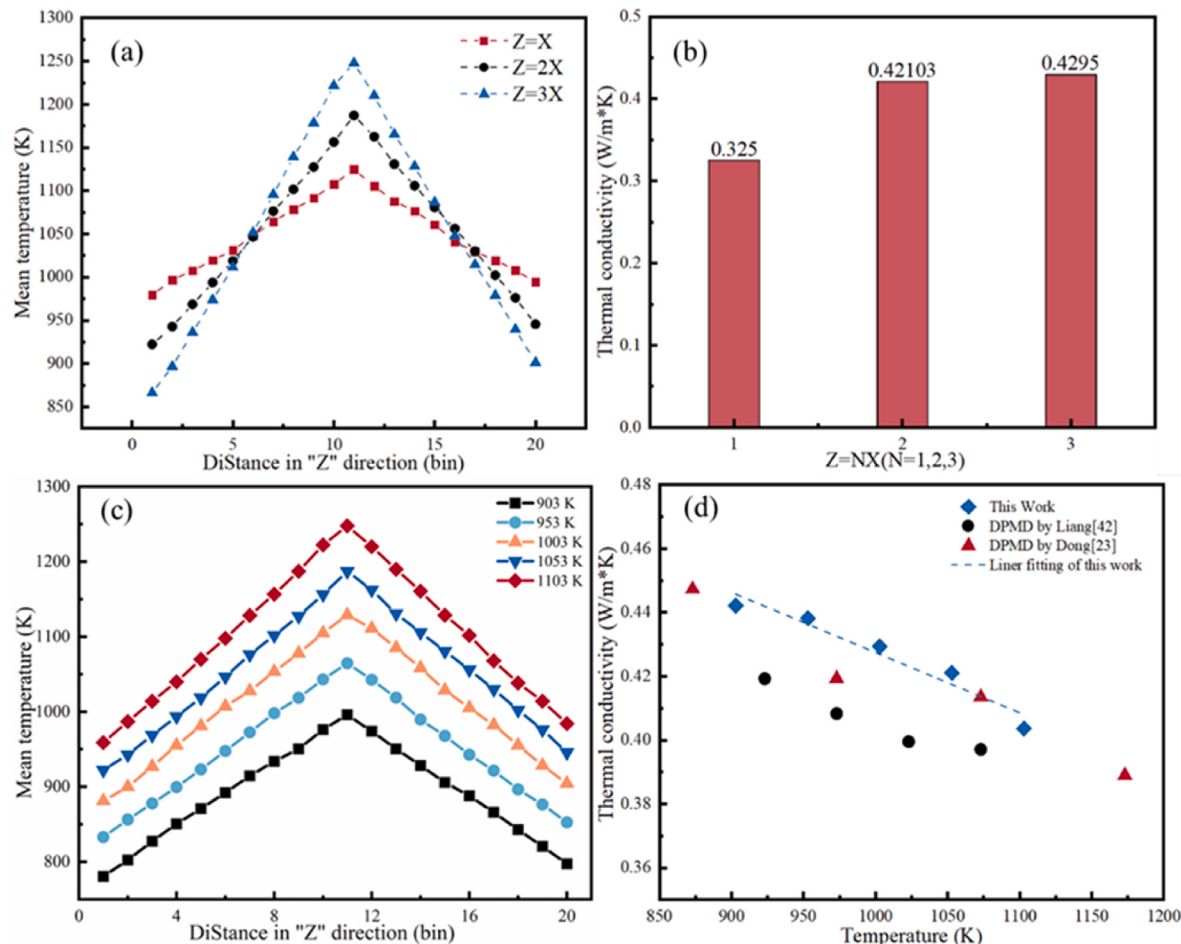


Fig. 10. (a) Average temperature gradient at 1053 K with Z = NX (N = 1, 2, 3), (b) Thermal conductivity at 1053 K with Z = NX (N = 1, 2, 3), (c) Average temperature gradient at different temperatures, where the solid line represents a linear fit of temperature. (d) Thermal conductivity calculated by DPMD. The solid blue square represents the calculated value of DPMD, and the dashed blue line represents the linear fitting curve. The black circle and the red upper triangle are respectively MgCl₂-NaCl calculated by Liang [42] and NaCl-MgCl₂-CaCl₂ thermal conductivity calculated by Dong [23].

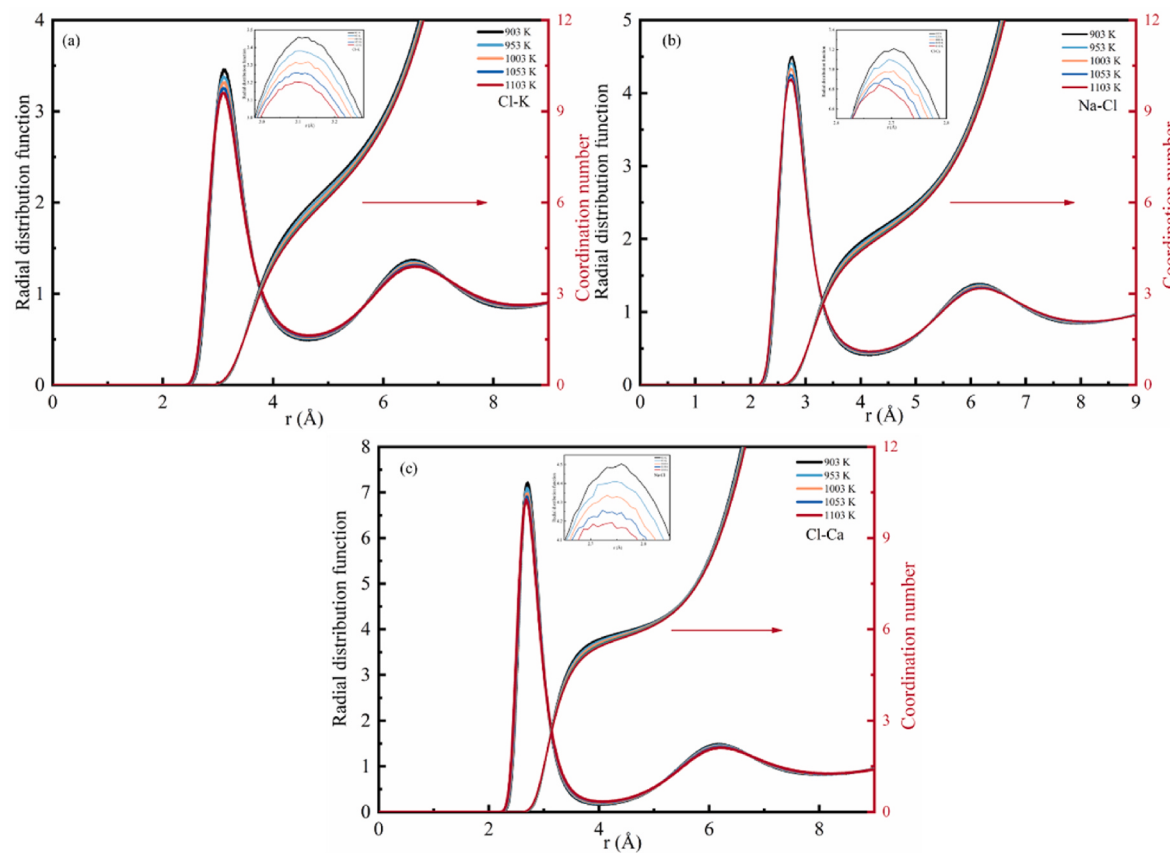


Fig. 11. Partial RDF and coordination number, (a) K-Cl, (b) Na-Cl, (c) Ca-Cl.

thermal conductivity exploration in the subsequent calculations. Fig. 10(c) depicts the temperature distribution along the z-axis, with a linear distribution between cold and hot sources. This linearity indicates that the system produces a stable temperature gradient between thermal extremes, thus ensuring the accuracy of the DPMD calculation. The thermal conductivity is shown in Fig. 10(d) and it is observed to be inversely proportional to the temperature. At 903 K, the thermal conductivity is 0.4422 W/(m·K), and it decreases to 0.4036 W/(m·K) at 1103 K. Furthermore, it can be observed that in the temperature range of 903–1103 K, the thermal conductivity of NaCl-KCl-CaCl₂ molten salt explored in this paper is slightly higher than that of MgCl₂-NaCl and NaCl-MgCl₂-CaCl₂, indicating that this molten salt has better heat transfer performance. The functional relationship with temperature is shown in Eq. (15), and its fitting coefficient is 0.9708, indicating that the model has strong correlation and prediction effect within the studied temperature range.

$$\lambda = 0.616 - 1.8865 \times 10^{-4} T \quad (15)$$

4.3. Structural analysis

4.3.1. Radial distribution function and coordination number

Fig. 11 presents the temperature-dependent variation of the RDF and CN for the NaCl-KCl-CaCl₂ system. A distinct first peak is observed in the RDF for all ion pairs, which shifts downwards and to the left with increasing temperature. The first peak decreases, indicating that the interaction between ions decreases with increasing temperature. Additionally, as the temperature rises, the interaction distance becomes shorter, which may lead to changes in the short-range local structure between neighboring ions. It may further cause the decrease of thermophysical properties density and viscosity, as shown in Figs. 7 and 8(b). The mean coordination numbers for the ion pairs also exhibit a downward trend to the right with temperature rise, indicative of a structural transition towards a more porous arrangement, which is consistent with the RDF observations. Table 5 compiles specific data related to the first peak and average coordination numbers for the molten salt ion pairs. The average coordination numbers for K-Cl, Na-Cl, and Ca-Cl ion pairs decrease from 6.98, 5.59, and 5.96 to 6.51, 5.25, and 5.78, respectively. This suggests that as temperature increases, ionic clusters tend to fragment into smaller clusters, leading to a decrease in structural order. The subsequent sections further corroborate this trend.

Table 5
RDF peak position, peak and average coordination number.

Temperature (K)	peak position			peak value			CN		
	Cl-K	Na-Cl	Cl-Ca	Cl-K	Na-Cl	Cl-Ca	Cl-K	Na-Cl	Cl-Ca
903	3.10	2.76	2.70	3.46	4.50	7.21	6.98	5.59	5.96
953	3.11	2.75	2.70	3.38	4.41	7.10	6.80	5.37	5.90
1003	3.13	2.73	2.70	3.32	4.34	6.98	6.81	5.52	5.90
1053	3.10	2.72	2.69	3.26	4.26	6.91	6.78	5.27	5.87
1103	3.09	2.74	2.68	3.20	4.19	6.84	6.51	5.25	5.78

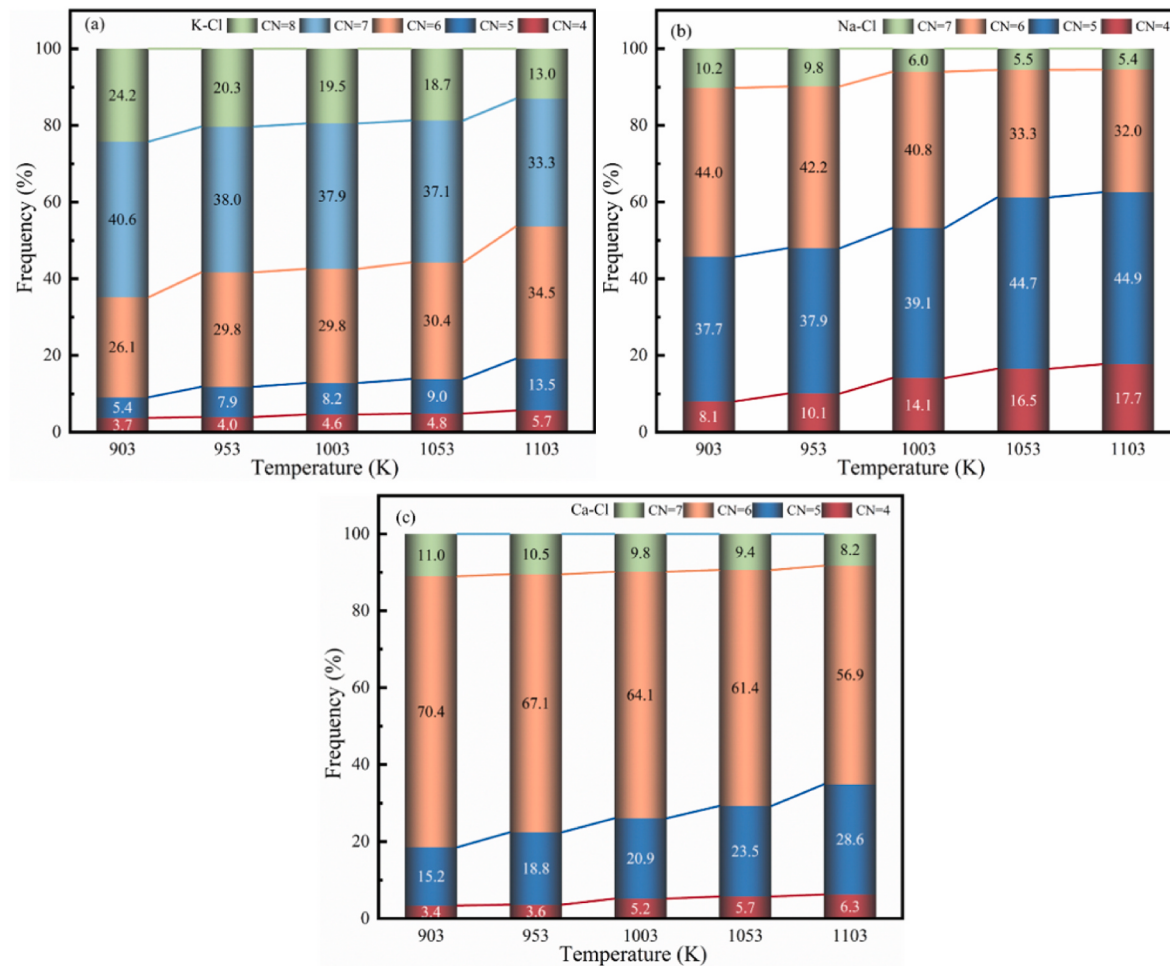


Fig. 12. Coordination number distribution, (a) K-Cl (b) Na-Cl (c) Ca-Cl.

with the proportion of different coordination numbers.

Fig. 12 further analyzes the distribution of coordination numbers (CN) for K-Cl, Na-Cl, and Ca-Cl ion pairs, revealing a decline in the proportion of high CN structures and an increase in low CN structures with rising temperature. For K-Cl pairs, the predominant CN structures are 7 at 903 K (40.6 %) and 6 at 1103 K (34.5 %). In the case of Na-Cl pairs, the CN primarily ranges from 4 to 7, with 5 and 6 CN structures accounting for 37.7 % and 44.0 % at 903 K, respectively. At 1103 K, the 5 CN structure peaks at 44.9 %, while the 6 CN structure decreases to 32 %. For Ca-Cl pairs, the 6 CN structure decreases from 70.4 % at 903 K to 56.9 % at 1103 K, while the 5 CN structure increases from 15.2 % to 28.6 %. These findings corroborate the trend of decreasing structural order in the molten salt system.

4.3.2. Angle distribution function and potential of mean force

The ADF of the NaCl-KCl-CaCl₂ molten salt system is shown in Fig. 13. In the structures of Cl-K-Cl, Cl-Na-Cl, and Cl-Ca-Cl, distinct double peaks are observed, with those associated with Cl-Ca-Cl being particularly pronounced. Over the studied temperature range, the primary peak in Cl-K-Cl transitions from 73.5° to 72.5°, accompanied by a relatively flattened peak occurring between 125° and 140°. Similarly, in Cl-Na-Cl, the peak shifts from 83.5° to 82.5°, with a corresponding flat peak evident between 140° and 160°. Conversely, the peaks in Cl-Ca-Cl are both narrower and more elevated, migrating from 84.5° to 82.5°, while the lower peak moves from 160° to 158.5°. Due to the octahedral characteristic peaks at 90° and 180° [24,43], this suggests that the structure of Ca ions in the molten salt may be a distorted polyhedron, and the distortion may intensify with increasing temperature.

Above, we analyzed the RDF and CN changes of mixed molten salts in the 903 K–1103 K temperature range, here, we analyzed the energy of Cl ions escaping the first coordination layer of K, Na, Ca, ions, corresponding to the difference between the first peak and the first peak valley in the curve. The acquisition of Fig. 14 in this paper primarily refers to the work of Dong [23]. The calculation of the Potential of Mean Force (PMF) is mainly based on Eq. (16), where the first term $\frac{1}{k_B T} W_{eff}(r)$ is defined as the PMF, which is primarily used to assess the activation energy barrier for the Cl ion to escape from the first coordination shell of the cations Ca, Na, and K. Here, $g_{ij}(r)$ is RDFS, T is the corresponding temperature, r_{min} corresponds to the position of the first minimum in the RDFS, k_B is Boltzmann's constant.

$$\frac{1}{k_B T} W_{eff}(r) = -\ln g_{ij}(r) - 2 \ln \left(\frac{r}{r_{min}} \right) \quad (16)$$

Fig. 14 delineates a decrement in the energy barrier height for all ion pairs. As the operating temperature rise, the energy barriers (Ebarriers) for K-Cl, Na-Cl, and Ca-Cl pairs decrease, so thermal elevation intensifies the kinetic activity of ions, thereby promoting the dissociation of Cl ions, and then molten salt gradually loses stability. The maximum energy barriers for the K-Cl, Na-Cl, and Ca-Cl pairs are recorded as 1.58, 2.02, and 3.29 kJ/mol, respectively, with the Ca-Cl pair demonstrating the most formidable binding energy. This discovery aligns with the elevated RDF peak observed in previous investigations for the Ca-Cl pair, affirming the stability of the Ca-Cl interaction.

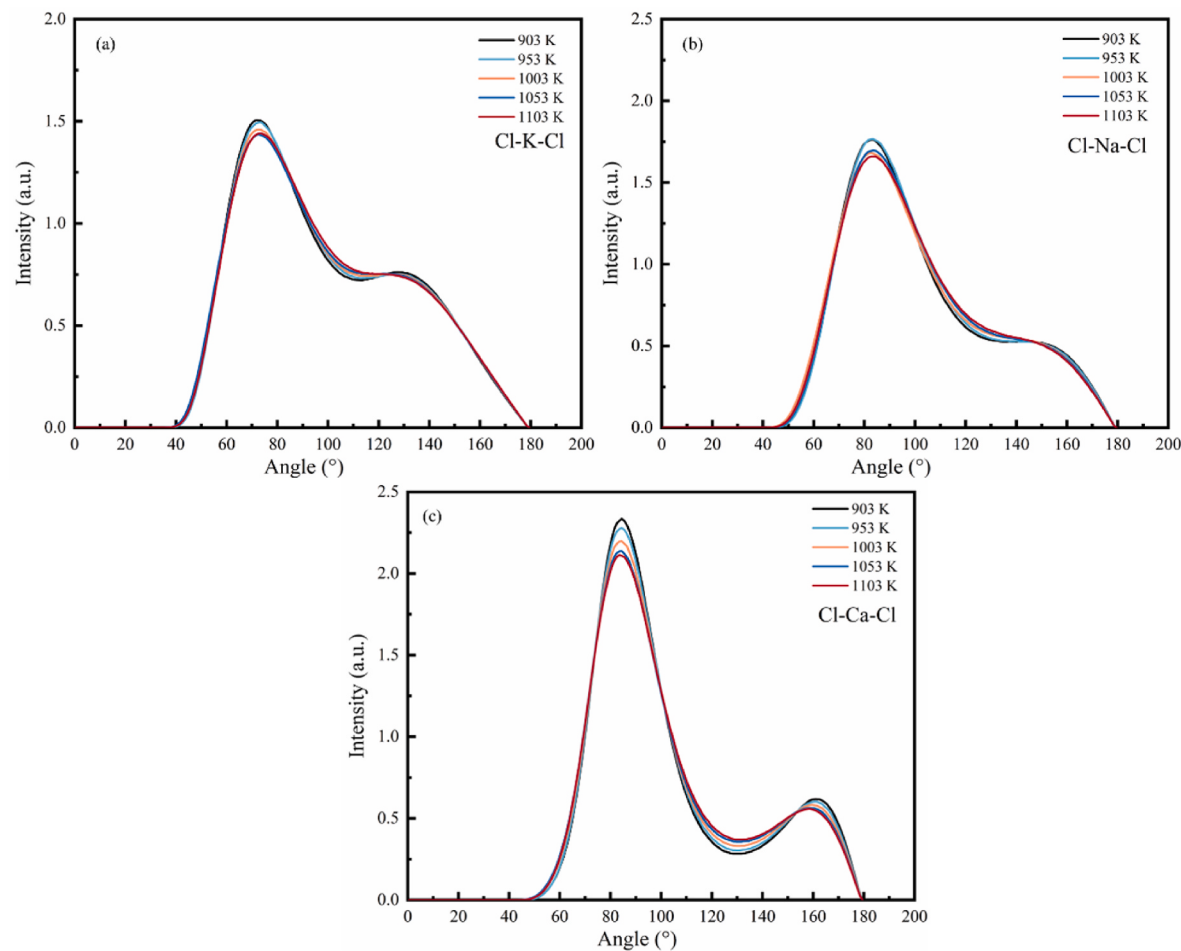


Fig. 13. Adf (a) Cl-K-Cl, (b) Cl-Na-Cl, (c) Cl-Ca-Cl.

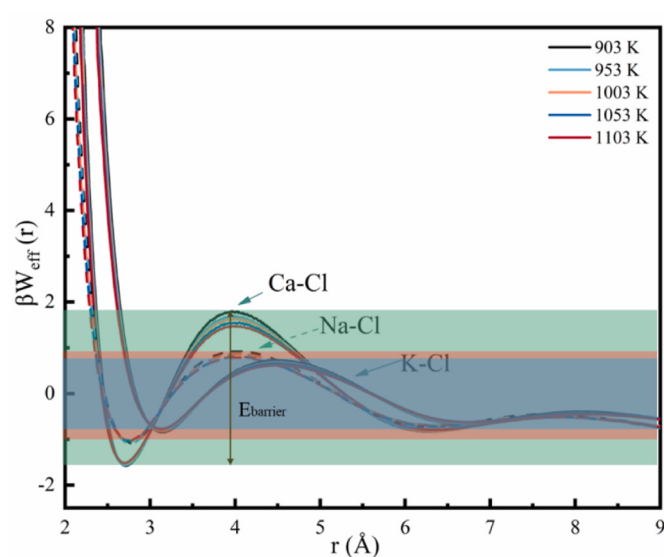


Fig. 14. Potential of mean force.

5. Conclusion

In this study, the thermophysical properties and microstructure of NaCl-KCl-CaCl₂ molten salt were investigated across a temperature range of 903 K–1103 K using DPMD and experiments. The main

conclusions are as follows.

1. The present NaCl-KCl-CaCl₂ molten salt system has high thermal storage density with melting enthalpy of 251.37 J/g and high thermal stability with observable evaporation at temperatures above 1103 K.
2. The trained DP model performs well with high accuracy. The energy and force data predicted by DPMD show good agreement with density functional theory (DFT) simulation results, with RMSE of 0.50 meV/atom and 15.31 meV/ \AA , respectively. The errors of density and viscosity between calculation and experiment are less than 5 %, which strongly proves the feasibility of DPMD in thermal performance prediction.
3. The correlation equations for density, specific capacity, thermal conductivity, and viscosity of present salt are derived, and the results show that there is a negative correlation with the temperature change.
4. The structural evolution dominates the thermal performance variation. As temperature increases, the interionic interaction forces among K-Cl, Na-Cl, and Ca-Cl pairs diminish, leading to a transition towards lower coordination numbers and a decline in structural orderliness, and the energy barriers for ion pairs drops, so properties (density and viscosity) and thermal stability decrease. Notably, the Ca ions exhibit the highest energy barriers, underscoring their enhanced binding affinity and resistance to thermal dissociation.

Generally, the research demonstrates the significant potential of DPMD simulations in the study of high-temperature molten salt materials, providing reliable theoretical guidance for the development and optimization of high-temperature thermal storage systems based on

molten salts.

CRediT authorship contribution statement

Xianqing Liu: Writing – review & editing, Writing – original draft, Visualization, Validation, Project administration, Methodology, Investigation, Formal analysis, Data curation, Conceptualization. **Fei Liang:** Writing – review & editing, Validation, Formal analysis, Data curation, Conceptualization. **Shule Liu:** Validation, Software, Methodology, Investigation. **Gechuanqi Pan:** Resources, Funding acquisition, Formal analysis, Data curation, Conceptualization. **Jing Ding:** Supervision, Resources, Methodology, Funding acquisition. **Jianfeng Lu:** Writing – review & editing, Visualization, Supervision, Resources, Investigation, Funding acquisition.

Declaration of competing interest

The authors declare that they have no known competing financial interests or personal relationships that could have appeared to influence the work reported in this paper.

Acknowledgements

This work is supported by National Natural Science Foundation of China (U22A20213, 52036011, 52106233).

Data availability

Data will be made available on request.

References

- [1] X. Xue, X. Liu, A. Zhang, et al., Performance and economic analysis of a molten salt furnace thermal energy storage and peaking system coupled with thermal power units for iron and steel gas waste heat recovery, *Appl. Energy* 363 (2024) 123021.
- [2] Q. Zhang, J. Dong, H. Chen, et al., Dynamic characteristics and economic analysis of a coal-fired power plant integrated with molten salt thermal energy storage for improving peaking capacity, *Energy* 290 (2024) 130132.
- [3] V.M.B. Nunes, M.J.V. Lourenço, F.J.V. Santos, et al., Molten alkali carbonates as alternative engineering fluids for high temperature applications, *Appl. Energy* 242 (2019) 1626–1633.
- [4] A. Bonk, S. Sau, N. Uranga, et al., Advanced heat transfer fluids for direct molten salt line-focusing CSP plants, *Prog. Energy Combust. Sci.* 67 (2018) 69–87.
- [5] G. Ji, J. Gu, Z. Chen, et al., Experimental research on heat transfer characteristic of HITEC molten salt in evacuated tube solar collector, *Front. Energy Res.* 11 (2023) 1150326.
- [6] G. Pan, X. Wei, C. Yu, et al., Thermal performance of a binary carbonate molten eutectic salt for high-temperature energy storage applications, *Appl. Energy* 262 (2020) 114418.
- [7] R. Raud, S. Bell, T.C. Ong, et al., Optimized salt selection for solar thermal latent heat energy storage, *Adv. Sustain. Syst.* 2 (2018) 1800074.
- [8] S. Sau, N. Corsaro, T. Crescenzi, et al., Techno-economic comparison between CSP plants presenting two different heat transfer fluids, *Appl. Energy* 168 (2016) 96–109.
- [9] H. Tian, W. Wang, J. Ding, et al., Thermal performance and economic evaluation of NaCl–CaCl₂ eutectic salt for high-temperature thermal energy storage, *Energy* 227 (2021) 120412.
- [10] Y. Wang, Y. Lu, Y. Wang, et al., Investigation on thermal performance of quinary nitrate/nitrite mixed molten salts with low melting point for thermal energy storage, *Sol. Energy Mater. Sol. Cell.* 270 (2024) 112803.
- [11] R. Jacob, M. Liu, Y. Sun, et al., Characterization of promising phase change materials for high temperature thermal energy storage, *J. Energy Storage* 24 (2019) 100801.
- [12] H. Na, C. Zhang, Y. Wu, et al., Investigation on thermal performance of eutectic binary nitrate-carbonate molten salt under thermal shock condition, *Sol. Energy Mater. Sol. Cell.* 255 (2023) 112314.
- [13] Y. Wang, Y. Lu, Y. Wang, et al., Investigation on thermal performance of quinary nitrate/nitrite mixed molten salts with low melting point for thermal energy storage, *Sol. Energy Mater. Sol. Cell.* 270 (2024) 112803.
- [14] T.C. Ong, M. Sarvghad, K. Lippiatt, et al., Investigation of the corrosion of electroless nickel-plated alloys in molten salt and its effect on phase change properties for energy storage applications, *Sol. Energy* 236 (2022) 512–521.
- [15] T. Ong, M. Sarvghad, K. Lippiatt, et al., Review of the solubility, monitoring, and purification of impurities in molten salts for energy storage in concentrated solar power plants, *Renew. Sustain. Energy Rev.* 131 (2020) 110006.
- [16] L. González-Fernández, M. Intxaurieta-Carcedo, O. Bondarchuk, et al., Effect of dynamic conditions on high-temperature corrosion of ternary carbonate salt for thermal energy storage applications, *Sol. Energy Mater. Sol. Cell.* 240 (2022) 111666.
- [17] H. Tian, Z. Kou, X. Pang, et al., Molecular dynamics simulation on thermophysical properties and local structure of ternary chloride salt for thermal energy storage and transfer system, *Energy* 284 (2023) 129277.
- [18] J. Ding, F. Gong, S. Yang, et al., Microstructure and thermal properties of NaCl-ZnCl₂ molten salt by molecular dynamics simulation and experiment, *Sol. Energy Mater. Sol. Cell.* 250 (2023) 112108.
- [19] Z. Huang, Q. Li, Y. Qiu, Enhancements in thermal properties of binary alkali chloride salt by Al₂O₃ nanoparticles for thermal energy storage, *Energy* 301 (2024) 131584.
- [20] K. Duemmler, D. Andersson, B. Beeler, First-principles investigation of the thermophysical properties of NaCl, PuCl₃, and NaCl-PuCl₃ molten salts, *J. Nucl. Mater.* 591 (2024) 154902.
- [21] S. Qi, T. Bo, L. Zhang, et al., Machine-learning-driven simulations on microstructure, thermodynamic properties, and transport properties of LiCl-KCl-LiF molten salt, *Artificial Intellig. Chem.* 2 (2024) 10002.
- [22] Y. Xie, M. Bu, Y. Zhang, et al., Effect of composition and temperature on microstructure and thermophysical properties of LiCl-CaCl₂ molten salt based on machine learning potentials, *J. Mol. Liq.* 383 (2023) 122112.
- [23] W. Dong, H. Tian, W. Zhang, et al., Development of NaCl-MgCl₂-CaCl₂ ternary salt for high-temperature thermal energy storage using machine learning, *ACS Appl. Mater. Interfaces* 16 (2024) 530–539.
- [24] Y. Xie, M. Bu, G. Zou, et al., Molecular dynamics simulations of CaCl₂-NaCl molten salt based on the machine learning potentials, *Sol. Energy Mater. Sol. Cell.* 254 (2023) 112275.
- [25] G. Kresse, J. Furthmüller, Efficiency of ab-initio total energy calculations for metals and semiconductors using a plane-wave basis set, *Comput. Mater. Sci.* 6 (1996) 15–50.
- [26] G.J.D. Kresse, From ultrasoft pseudopotentials to the projector augmented-wave method, *Phys. Rev. B* 59 (1999) 1758.
- [27] P.E. Blochl, Projector augmented-wave method, *Phys. Rev. B* (1994) 17953–17979.
- [28] M. Bu, W. Liang, G. Lu, et al., Local structure elucidation and properties prediction on KCl–CaCl₂ molten salt: a deep potential molecular dynamics study, *Sol. Energy Mater. Sol. Cell.* 232 (2021) 111346.
- [29] W. Liang, J. Wu, H. Ni, et al., First-principles molecular dynamics simulations on the local structure and thermo-kinetic properties of molten magnesium chloride, *J. Mol. Liq.* 298 (2020) 112063.
- [30] S. Grimme, Semiempirical GGA-type density functional constructed with a long-range dispersion correction, *J. Comput. Chem.* 27 (2006) 1787–1799.
- [31] T. Bucko, J. Hafner, S. Lebegue, et al., Improved description of the structure of molecular and layered crystals: ab initio DFT calculations with van der Waals corrections, *J. Phys. Chem.* 114 (2010) 11814–11824.
- [32] F. Liang, J. Ding, X. Wei, et al., Interfacial heat and mass transfer at silica/binary molten salt interface from deep potential molecular dynamics, *Int. J. Heat Mass Tran.* 217 (2023) 124705.
- [33] Y. He, Y. Qiu, K. Wang, et al., Perspective of concentrating solar power, *Energy* 198 (2020) 117373.
- [34] H. Wang, L. Zhang, J. Han, et al., DeepMD-kit: a deep learning package for many-body potential energy representation and molecular dynamics, *Comput. Phys. Commun.* 228 (2018) 178–184.
- [35] H. Yin, Z. Wang, X. Lai, et al., Optimum design and key thermal property of NaCl-KCl-CaCl₂ eutectic salt for ultra-high-temperature thermal energy storage, *Sol. Energy Mater. Sol. Cell.* 236 (2022) 111541.
- [36] M.M. Kenisarin, High-temperature phase change materials for thermal energy storage, *Renew. Sustain. Energy Rev.* 14 (2010) 955–970.
- [37] M. Bu, W.S. Liang, G. Lu, et al., Molecular dynamics simulations on AlCl₃-LiCl molten salt with deep learning potential, *Comput. Mater. Sci.* 210 (2022) 111494.
- [38] G. Pan, J. Ding, P. Chen, et al., Finite-size effects on thermal property predictions of molten salts, *Sol. Energy Mater. Sol. Cell.* 221 (2021) 110884.
- [39] G.C. Pan, J. Ding, W. Wang, et al., Molecular simulations of the thermal and transport properties of alkali chloride salts for high-temperature thermal energy storage, *Int. J. Heat Mass Tran.* 103 (2016) 417–427.
- [40] J. Lu, S. Yang, G. Pan, et al., Thermal and transport properties of molten chloride salts with polarization effect on microstructure, *Energies* 14 (2021) 746.
- [41] G.J. Janz, R.P.T.T. Tomkins, Physical properties data compilations relevant to energy storage. II. Molten Salts: Data on Singleand Multi-Component Salt Systems, 1981, pp. 1–882.
- [42] W. Liang, G. Lu, J. Yu, et al., Machine learning accelerates molten salt simulations: thermal conductivity of MgCl₂-NaCl Eutectic, *Adv. Theor. Simulat.* 5 (2022) 2200206.
- [43] M. Bu, W.S. Liang, G.M. Lu, et al., Static and dynamic ionic structure of molten CaCl₂ via first-principles molecular dynamics simulations, *Ionics* 27 (2021) 771–779.